



Imaging subsurface migration of dissolved CO₂ in a shallow aquifer using 3-D time-lapse electrical resistivity tomography



Esben Auken^a, Joseph Doetsch^{a,*}, Gianluca Fiandaca^a, Anders Vest Christiansen^a, Aurélie Gazoty^a, Aaron Graham Cahill^b, Rasmus Jakobsen^c

^a Department of Geosciences, Aarhus University, Aarhus, Denmark

^b Department of Environmental Engineering, Technical University of Denmark, Copenhagen, Denmark

^c GEUS—Geological Survey of Denmark and Greenland, Copenhagen, Denmark

ARTICLE INFO

Article history:

Received 26 September 2013

Accepted 27 November 2013

Available online 4 December 2013

Keywords:

ERT

Monitoring

Time-lapse inversion

CO₂

Groundwater

Electrical resistivity

ABSTRACT

Contamination of groundwater by leaking CO₂ is a potential risk of carbon sequestration. With the help of a field experiment in western Denmark, we investigate to what extent surface electrical resistivity tomography (ERT) can detect and image dissolved CO₂ in a shallow aquifer. For this purpose, we injected CO₂ at a depth of 5 and 10 m and monitored its migration using 320 electrodes on a 126 m × 25 m surface grid. A fully automated acquisition system continuously collected data and uploaded it into an online database. The large amount of data allows for time-series analysis using geostatistical techniques for noise estimation and data interpolation to compensate for intermittent instrument failure. We estimate a time-dependent noise level for each ERT configuration, taking data variation and measurement frequency into account.

A baseline inversion reveals the geology at the site consisting of aeolian and glacial sands near the surface and marine sands below 10 m depth. 3-D time-lapse ERT inversions clearly image the dissolved CO₂ plume with decreased electrical resistivity values. We can image the geochemical changes induced by the dissolved CO₂ until the end of the acquisition, 120 days after the injection start. During these 120 days, the CO₂ migrates about 25 m in the expected groundwater flow direction. Water electrical conductivity (EC) sampling using small screens in 29 wells allows for very good verification of the ERT results. Water EC and ERT results generally agree very well, with the water sampling showing some fine-scale variations that cannot be resolved by the ERT. The ERT images have their strength in outlining the plume's shape in three dimensions and in being able to image the plume outside the well field. These results highlight the potential for imaging dissolved CO₂ using non-intrusive surface electrical resistivity tomography.

© 2013 Elsevier B.V. All rights reserved.

1. Introduction

Geological carbon sequestration is a promising technique for reducing CO₂ release into the atmosphere by capturing the CO₂ (e.g., at power plants) and injecting it into deep reservoirs for long-term storage. Potential storage formations are abandoned oil and gas fields, saline formations and coal beds (Benson et al., 2005). Irrespective of the storage formation, the reservoirs must be sealed by several layers of fully intact cap rock that prevent leakage into shallow formations. The risk of leakage from properly chosen reservoirs with adequate cap rock is very small. Nevertheless, it is important to monitor the migration of the CO₂ for the safe and efficient operation of underground CO₂ storage (Benson et al., 2005).

Efficient operation of the CO₂ injection requires monitoring and simulation of the migrating CO₂ in the reservoir. Monitoring outside

the reservoir is mostly important for leakage detection and serves regulatory as well as public perception purposes. Although unlikely, the increased reservoir pressure can lead to leakage of reservoir brine (high salinity water) or CO₂ into shallow aquifers (Birkholzer et al., 2009). Therefore, before permitting any geological CO₂ storage, monitoring strategies for leaked brine and CO₂ need to be in place. Brine leakage is often considered more critical and its modeling (Nicot, 2008) and detection (Günther et al., 2013) is currently being investigated. Reservoir brine is mostly of high salinity and can therefore increase salinity levels in groundwater above acceptable drinking water limits. At the same time, leaked brine is characterized by a strong decrease in electrical resistivity, due to the dissolved salt. Here, we concentrate on monitoring the CO₂ itself and not the brine it is replacing.

Under reservoir conditions with temperatures above 31 °C and pressures above 73.8 bars, CO₂ exists in a supercritical phase, which partly behaves like a fluid, partly like a gas. The potential of geophysical methods for monitoring of supercritical CO₂ in the reservoir has been demonstrated in several pilot storage studies (e.g., Giese et al., 2009;

* Corresponding author at: Hydrogeophysics Group, Aarhus University, C. F. Møllers Allé 4, DK-8000 Aarhus, Denmark. Tel.: +45 87162373.

E-mail address: joseph.doetsch@geo.au.dk (J. Doetsch).

Hovorka et al., 2006, 2011). These studies used crosswell installations to measure the change in seismic velocity (e.g., Ajo-Franklin et al., 2013) or electrical resistivity (Carrigan et al., 2013; Doetsch et al., 2013; Schmidt-Hattenberger et al., 2013) that was induced by injected supercritical CO₂. The advantage of these geophysical methods is the comparably high spatial resolution at the interwell scale of tens of meters and the sensitivity to changes in bulk properties, such as supercritical-phase or gas saturation.

While only few examples show the potential of geophysical reservoir monitoring, even fewer examples of geophysical leak detection and monitoring of CO₂ in shallow aquifers exist. Only very few studies (Dafflon et al., 2013; Lamert et al., 2012; Strazisar et al., 2009) have investigated the electrical signature of dissolved CO₂ in groundwater. Both Lamert et al. (2012) and Dafflon et al. (2013) find that electrical resistivity initially decreases after the CO₂ injection, due to an increase of bicarbonate and dissolved species. Dafflon et al. (2013) also find that as pH decreases further, resistivity rebounds toward initial conditions, due to a reduction of dissociated species. While they observe changes in resistivity adjacent to the equipped boreholes, limitations in their setup prohibit Dafflon et al. (2013) from fully imaging the extent and shape of the dissolved CO₂ plume. We are trying to overcome this limitation by using 3-D surface electrical resistivity tomography (ERT) monitoring of dissolved CO₂ in a shallow aquifer.

Surface and crosswell ERT monitoring has been successfully used for solute transport monitoring in a number of studies (e.g., Binley et al., 2002; Cassiani et al., 2006; Doetsch et al., 2012b; Kemna et al., 2002; Singha and Gorelick, 2005; Slater et al., 2000). The main advantage of surface ERT monitoring is its applicability on the relevant horizontal groundwater flow scale of 50–100 m. Surface ERT monitoring has been reported to image salt tracers down to a depth of about 20 m (Robert et al., 2012) and recent studies showed its potential for monitoring of heat tracer tests (Hermans et al., 2012) with a possible application to hydrothermal systems. Surface ERT monitoring is also minimally invasive and largely automated, which facilitates long term monitoring. However, most instruments currently on the market are not designed to withstand the wear of continuous long-term acquisition, so that many projects suffer from gaps in the ERT time-series due to intermittent instrument failure. The limitations of surface ERT monitoring of groundwater systems relate to the non-uniqueness of the geophysical response. For example, moisture content variations in the unsaturated zone can cause strong near-surface resistivity variations, which can mask groundwater related changes at greater depth (Coscia et al., 2012). More generally, each ERT data set can be explained by a large number of models and the inversion should be constrained

by other geophysical methods or geological knowledge wherever possible (e.g., Doetsch et al., 2012a).

In this contribution, we describe 3-D surface ERT monitoring of dissolved CO₂ in a shallow aquifer (2–10 m depth). We simulate leaked CO₂ from a deep reservoir by injecting food-quality CO₂ at 5 and 10 m depth into an aquifer near the west coast of Denmark. A pilot study at the same site (Cahill and Jakobsen, 2013) demonstrated that there is a clear decrease of water resistivity (about 30%) caused by dissolved CO₂, so that a clear resistivity signal could be expected in the ERT monitoring. Our geophysical monitoring was embedded into an extensive hydrological monitoring program (Cahill et al., under review) that analyzed the geochemical effects of the injected CO₂ on groundwater quality.

We first describe the field site and experiment (Section 2), before introducing our field installation and instrument setup that was specifically designed for this study (Section 3.1). Special preprocessing (Sections 3.2 & 3.3) was necessary before inverting the baseline and monitoring ERT data (Section 4). Finally, we interpret and discuss the ERT results with the help of the hydrological measurements (Section 5).

2. Field site and experiment near Esbjerg, Denmark

2.1. Hydrogeological setting

A shallow aquifer field site near Esbjerg in western Denmark (see inset in Fig. 1) was chosen for the CO₂ injection experiment. The field site is located about 6 km from Denmark's west coast and the geology is dominated by sands, partly with some portion of gravel or clay. Fig. 1 shows an aerial photograph of the field site that consists of a grassy clearing (center) and two forested regions. The coordinate system in Fig. 1 is used throughout this article; it has its origin at the CO₂ injection points at lat/lon: 55° 39.029' N, 8° 14.293' E and it is rotated 240° from north. Surface topography is relatively flat at an elevation of 15 m, with a few sand dunes in the forested region towards southwest ($x = 60$ – 80 in Fig. 1).

The top 5 m of the subsurface (elevation ~ 10–15 m) consists of fine aeolian sand, overlain by a thin layer of topsoil. The aeolian sand is underlain by glacial melt water sand between 5 and 10 m depth (~5–10 m elevation), followed by fine marine sand below 10 m depth (5 m elevation). The groundwater table is relatively stable and slightly falling from 1.5 m depth in the spring to 2 m in the fall. The hydraulic gradient is relatively low at 0.0014, falling towards south-southwest. Results of a pilot study (Cahill and Jakobsen, 2013) were used for the planning of the main field experiment and confirmed the layered geology.

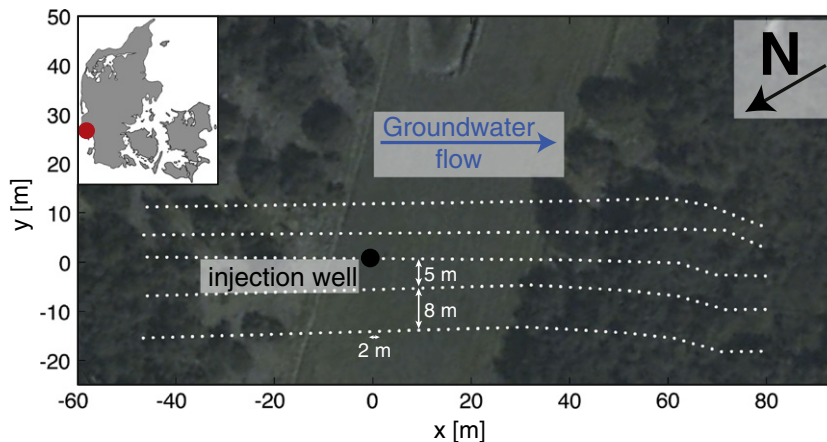


Fig. 1. Aerial photo of the field site near Esbjerg and its location in Denmark (see inset). A total of 320 electrodes (white dots) were permanently installed in an area covering 126 m by 25 m. The same local coordinate system with its origin at the injection well is used in all Figures. Image source: maps.google.com.

2.2. CO₂ injection experiment

The CO₂ injection experiment was designed to simulate CO₂ leakage in the shallow subsurface at 5–10 m depth and monitor its migration by both water sampling and surface electrical resistivity tomography (ERT). The CO₂ was injected in a total of four screened borehole intervals in two wells at 4–5 and 9–10 m depth at the locations $x = 0$ and $y = \pm 1$ m to create a curtain of CO₂ perpendicular to the groundwater flow direction (Cahill et al., under review).

Injection of gas phase, food-quality CO₂ started on May 14th 2012 at the rate of 12 L/min. All timing information is given with respect to this injection start on May 14th 2012. After 14 days of injection and the detection of complete water desaturation at some sampling points, the injection rate was reduced to 6 L/min (16 kg CO₂/day). CO₂ injection continued at this constant rate until July 24th, for a total injected CO₂ amount of 1600 kg in 72 days.

2.3. Water sample analysis

The water sampling campaign of Cahill et al. (under review) was targeted at finding a reliable indicator for leaked CO₂ in a freshwater aquifer as well as monitoring geochemical changes and water quality changes induced by the CO₂. 29 monitoring wells were installed between $x = -1$ m and $x = 20$ m and $y = -4$ m to $y = 4$ m, with the groundwater flow direction approximately parallel to the x -axis. The water sampling positions in most boreholes were located at 2 m (just below the water table), 4 m and 8 m depth. Water samples were taken before the beginning of the CO₂ injection and 10 times within the first 120 days after beginning the injection. Each water sample was tested for electrical conductivity (EC), pH, dissolved oxygen, alkalinity, Si, major and minor cation concentrations. The EC was used to check for errors in major cation concentrations assuming a near constant relation between EC and total sum of cationic charges. Except for HCO₃⁻, changes in anion concentrations were not expected, and only a few samples were also analyzed for major anions, confirming expectations as changes were within the range seen in the background samples taken prior to the CO₂ injection.

A pilot study (Cahill and Jakobsen, 2013) found that electrical conductivity was the most stable indicator for migrated CO₂. Cahill et al. (under review) confirm this result and additionally find that the advectively moving CO₂ first elevates concentration with a peak especially in Mg, Ca, Na, Al and HCO₃⁻, followed by increasing acidification and a continued elevated concentration of the mentioned ions. While disentangling geochemical signatures and monitoring of dissolved element concentrations are important for water quality analysis, we concentrate here on the water conductivity measurements that relate directly to the ERT measurements.

3. ERT monitoring setup and data acquisition

3.1. Surface ERT layout and instrument setup

A total of 320 stainless steel electrodes were installed in 5 lines (64 electrodes each), to continuously monitor the subsurface electrical resistivity. Each electrode was placed in a bentonite-filled hole at the surface to ensure low contact resistances in the sandy environment. The ERT grid covered an area of 126 × 25 m, with the long axis approximately parallel to the groundwater flow direction (Fig. 1). The inline electrode spacing was 2 m, with a line spacing of 5–8 m. 3-D coverage was ensured by inline as well as crossline measurements. The groundwater flow direction was determined before the experimental design and due to the homogeneous sandy geology, groundwater flow was expected to be homogeneous and to not change direction over time. Under these circumstances, the lines parallel to the flow direction allow longer and more detailed imaging of the plume.

The acquisition, control and communication system (Fig. 2) was specifically designed for stand-alone monitoring, with as little user interaction as possible. While the general location of the field site at Denmark's west coast is not remote, the unavailability of electrical power or cabled communication connections asked for special design of the monitoring system. Power was provided by an uninterrupted power supply (UPS), consisting of a gasoline powered AC generator, four 120 Ah 12 V car batteries and a buffering and control system. The control system always charged two batteries, while the other two batteries were used for acquisition; capacitors acted as voltage buffers at the battery switching moments.

The actual acquisition system consisted of a field computer, a 10-channel Iris Instruments Syscal® with inbuilt 64-channel switching capability and 5 switch boxes (SB1–5 in Fig. 2) developed in-house. The switch boxes enabled automatic data acquisition with all 320 electrodes using a resistivity meter designed for only 64 electrodes. The resistivity meter was connected to the first switch box with two 32-channel multi-core cables and could always reach two sets of 32 electrodes. Each switch box has two 32-channel inputs and each input has two possible outputs: either a connection to the next switch box or a set of 32 electrodes connected to the switch box through a multi-core cable. Fig. 2 illustrates how cabling the switch boxes in alternating directions enables three types of layouts. It is possible to a) have one complete 64-electrode line active (Fig. 2a), b) acquire 3-D data between cables on the same survey side or c) get 3-D coverage by activating cables on different lines and survey sides.

All switch boxes, as well as the resistivity meter, were directly controlled by a field computer, which continuously cycled through a sequence of 25 cable combinations. The computer activated the specific cables by instructing the switch boxes and instructed the resistivity meter to acquire data using electrode combinations optimized for those cables. After complete acquisition of a data set, the computer archived the data and continued by measuring the next cable combination. While acquiring one data set, archived data was automatically uploaded to an online database on servers at Aarhus University. The online database was accessed through wireless communication, which could also be used to remotely access the computer for system checks or for changing acquisition settings and schedule.

The installed system offers a cost effective and flexible way to use a 64-channel resistivity meter with many more electrodes. The system can easily be extended to as many switch boxes as desired and the cost for each switch box is relatively low, because it only contains two switches for 32-channel cables, and individual channels do not need to be individually switched. The switch boxes were custom designed for this project, but are expected to be used in future projects, where large electrode numbers are important.

3.2. Data acquisition

The ERT acquisition system was installed in April 2012. Data acquisition commenced on April 27th, more than two weeks prior to the beginning of the CO₂ injection. Fig. 3 shows the daily number of acquired data points. While the maximum number of data per day is ~18,000, various problems with the Syscal resistivity meter (e.g. unstable power supply, unstable hardware, unstable firmware and unstable controlling software) caused some acquisition interruptions. Most failures could be fixed in a timely manner, but some needed external instrument repair and created data gaps of up to 20 days. Even with some gaps, more than 650,000 data points were acquired within the first 120 days after the start of the CO₂ injection.

The acquired data included gradient and dipole–dipole configurations on each of the five 64-electrode lines, as well as equatorial dipole–dipole data for parallel lines. For the offset lines as in Fig. 2c, the acquired data consisted mostly of measurements with one current

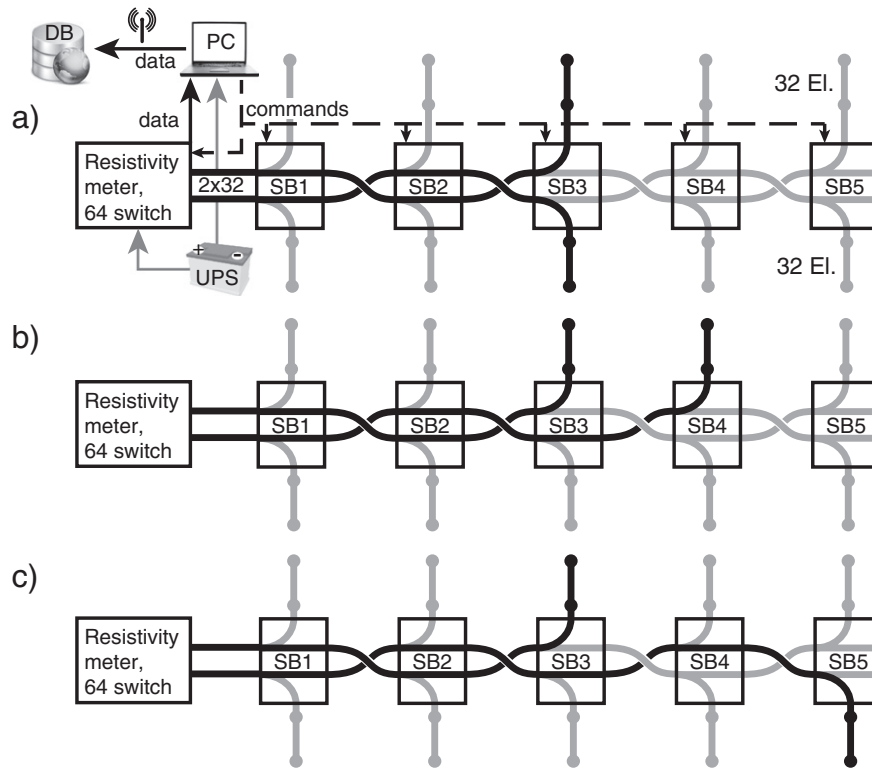


Fig. 2. Field system setup for fully automatic data acquisition using 320 electrodes with a 64-input resistivity meter. A field computer (PC) controls a 10-channel Syscal® resistivity meter and 5 switch boxes (SB1–5). Due to the alternating direction of the switch boxes (crossing cables), switches can be set to either acquire data on a) a single 64-electrode line, b) two cables on the same survey side or c) cables on different lines and different sides of the survey.

electrode on each line and potential electrodes both on the same and different lines. All measurements were optimized for the specific 10-channel resistivity meter, speeding up the acquisition by a factor of 8 compared to a single channel system.

The total number of 9640 four-electrode configurations consisted of 1380 measurements (900 gradient and 480 dipole–dipole) for each of the five profiles and 2740 3-D configurations across lines. Data were

acquired using a square waveform with a 2 s on-time and a stacking over 2 waveform cycles. The average injected current was 125 mA, the average measured voltage 544 mV and the mean geometrical factor for all configurations was 588 m. Induced polarization (IP) decay curves (20 gates) were also acquired for each direct current measurement. In this study, we concentrate on the direct current resistance measurements and the IP data will be processed at a later stage.

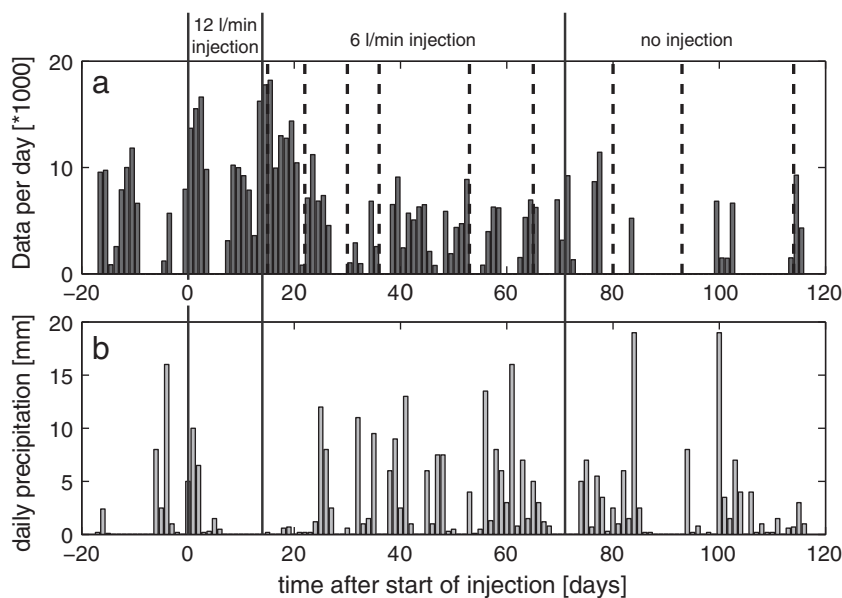


Fig. 3. Timeline of the experiment with the number of acquired ERT data per day (a) and the daily precipitation at the Esbjerg field site (b). Times are shown with respect to the beginning of the CO₂ injection on May 12th 2012. The initial injection rate of 12 l/min was reduced to 6 l/min after 14 days of injection. Dotted lines in (a) mark the times of water conductivity sampling in boreholes (see Sections 2.3 and 5.2). Data acquisition was compromised by intermittent instrument failures that resulted in some large gaps in the ERT time-series.

3.3. Preprocessing

Prior to inversion of the acquired time-lapse ERT data, it was preprocessed for quality control, outlier detection, and noise estimation. The large amount of data allows for a detailed time-series analysis, but it also necessitates automatic processing and outlier detection. The filtering and analysis functions and their parameters were therefore carefully chosen and tested on subsets of the data set.

3.3.1. Quality control and filtering

The 650,000 resistance measurements were first resorted into time-series for each of the 9640 four-electrode configurations. The average number of measurements per configuration was 67 and time-series with less than 40 data points recorded during the full experiment were excluded from further processing. Additionally, 300 dipole–dipole configurations with geometrical factors of $k > 10,000\text{m}$ were found to have low measurement voltages and poor quality and were thus removed. The remaining 8719 time-series were filtered for outliers by assuming that resistances vary smoothly with time. Visual inspection showed that no smooth time-series varied more than a factor of 2 from its median value, so all data points outside this range were removed. Further outlier detection used local and global standard deviations to judge the distance of an individual data point from the time-series. The sources for these outliers were mainly temporarily unconnected electrodes (e.g., due to electrode-chewing animals).

After outlier detection, time-series with strong oscillations were removed from the data set as well. These time-series were found by comparing the sum of absolute changes over the full survey time to the maximum variation. Time-series with the accumulated changes exceeding the maximum variation by more than a factor of 8 were deleted.

In a next step, reciprocal measurements were combined. Reciprocal measurements exist only for the dipole–dipole type configurations, because the reciprocal measurements for gradient-type configurations cannot be optimized for multiple channels and would have needed excessive acquisition time. In some cases, where the quality of the two reciprocal time-series was comparable, they were combined into a single time-series. In cases with strong quality differences, only the higher quality time-series was used for further processing. We found that it was important first to compile the two reciprocal time-series for outlier detection and quality control, instead of directly combining reciprocal measurements into a single time-series or comparing individual reciprocal measurements. In many cases, there was a consistent shift between the reciprocal time-series that would have otherwise been classified as random noise. The quality control resulted in 520,000 individual measurements in 7713 time-series that were used in the further processing.

3.3.2. Geostatistical time-series interpolation

In order to compensate for irregular acquisition intervals and for gaps in the data acquisition, we interpolated the ERT data using one-dimensional geostatistical tools (Kitanidis, 1997), implemented in the software package Gstat (Pebesma and Wesseling, 1998). In the geostatistical analysis, acquisition time was used as “location” and the logarithm of measured resistances as input data. We first analyzed the time-series by calculating and fitting variograms to each “type” of ERT configuration. A “type” is here characterized by its distances between the four electrodes, but not by the location within the survey grid. This resulted in 25 gradient and 7 dipole–dipole variograms, each with a high number of lag samples ($>100,000$) and further 150 variograms for the 3-D measurements with low sample numbers. All of the highly sampled variograms can be explained with a spherical variogram with no nugget effect and a range of 35 days. The sill (amplitude) varies strongly between the different variograms, but could be reliably fitted when the range was fixed, even for the poorly sampled

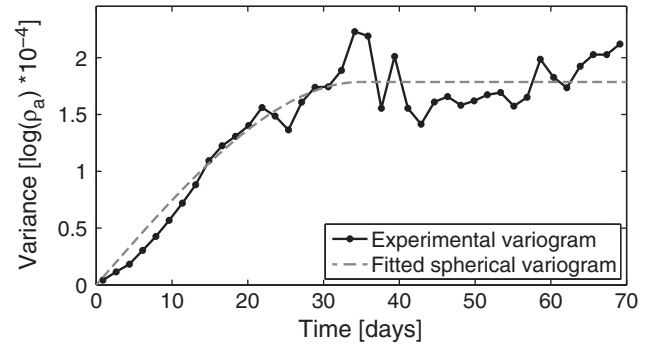


Fig. 4. Typical experimental and fitted variogram for gradient-type configurations. All 188 configurations with a current electrode spacing of 52 m, a potential electrode spacing of 4 m and a distance of 22 m between the closest current and potential electrodes were used to compile the experimental variogram.

variograms. A typical experimental and fitted variogram for gradient type configurations is shown in Fig. 4.

Ordinary kriging was then used to interpolate data for continuous coverage using the filtered time-series and the estimated variograms. Relative measurement errors of 0.5–1.5% were used for the kriging input, estimated for each time-series from the ratio of the accumulated changes and the maximum variation. The kriging outputs are resistance data at arbitrary times (e.g., daily) and data uncertainty, taking the time-coverage into account. Fig. 5 shows two interpolated time-series, estimated uncertainties and the underlying raw data. In this context, the advantage of kriging compared to other interpolation algorithms is the way it deals with irregular acquisition times. At highly sampled time intervals with very dense, possibly conflicting measurements, kriging yields weighted averages at the interpolation time. For interpolation times that are far from any actual measurements, high estimated errors reflect the interpolation uncertainty. For long time periods without any data, neither the kriging nor any other interpolation method can create data that contains additional information. The strength of the kriging is most pronounced at times with partial data coverage, where it gives high weight to sampled data points and down weights ERT configurations that only exist at larger time distances. An alternative to

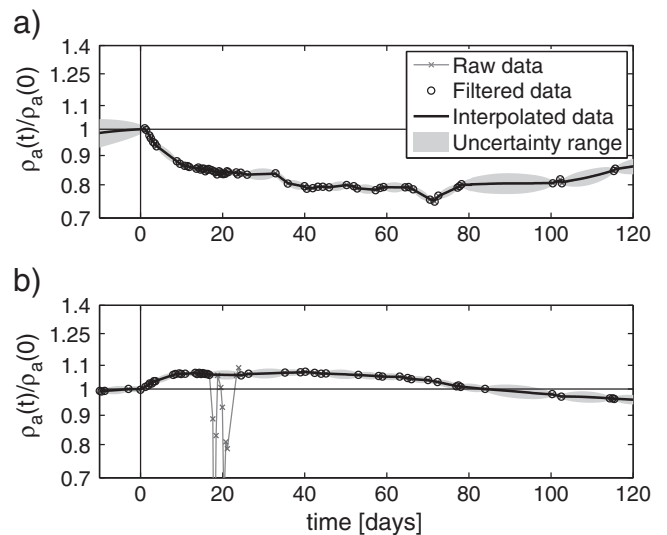


Fig. 5. Raw, filtered and interpolated normalized apparent resistivities, including the estimated error on the interpolated data. We first exclude clear outliers and use kriging with the remaining data to fill gaps in the time-series. The two curves show data from an example dipole–dipole (a) and gradient (b) configuration in the vicinity of the injection well. The quality of these two curves is much higher than for most other ERT configurations (see e.g., Fig. 6).

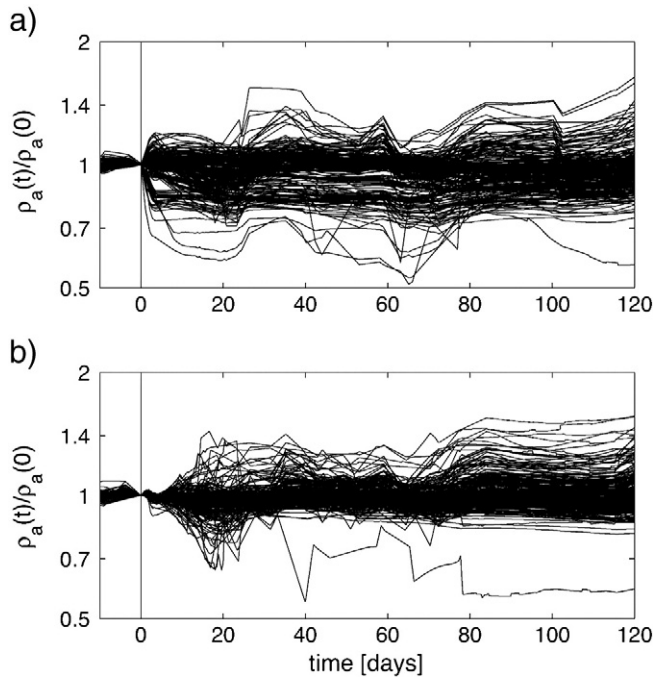


Fig. 6. Interpolated normalized apparent resistivity time-series centered around $x = 0$, for a) the center profile through the injection point and b) the profile farthest to the southwest (at $y = -15$). The time-series in a) show a clear change mostly to lower resistances directly after the start of the injection at day 0. The time variation in the data from the profile away from the injection point (b) is not coherent and mostly originates from near surface resistivity variations unrelated to the injected CO_2 .

kriging could have been to only select data in intervals with full coverage and then interpolate in the model space. However, inversion is another data transformation and we find it better to do the interpolation as close to the original data as possible.

Fig. 6 shows the kriged time-series for configurations centered around the injection well (Fig. 6a) and on the parallel line farthest to the southwest (Fig. 6b). Most time-series with the midpoint around the injection well show a clear effect of the injected CO_2 , directly after the injection start on day 0. Groundwater resistivity is expected to decrease as a result of the dissolved CO_2 and some apparent resistivity time-series show a decrease, while others show an increase following

the initial CO_2 injection. This seemingly contradictory apparent resistivity response highlights the complicated sensitivity pattern of ERT measurements and the necessity for time-lapse ERT inversions. The ERT time-series in Fig. 6b are not influenced by the injected CO_2 at early times and show the data variation due to noise and near-surface resistivity variations. Near-surface variations are mostly expected due to water saturation changes in the unsaturated zone following precipitation.

4. 3-D baseline and time-lapse ERT inversions

4.1. Mesh generation and baseline resistivity model

State of the art ERT modeling and inversion codes allow for a wide variety of discretization and regularization options (e.g., Günther et al., 2006). For example, unstructured meshes allow arbitrary topography and subsurface structure to be included in the inversion mesh and regularization can be decoupled at known interfaces (Doetsch et al., 2012a). We use an unstructured tetrahedral mesh and include surface topography, the groundwater table and one additional subsurface region in the mesh (Fig. 7). Electrode positions were measured with differential GPS, and surface topography is interpolated linearly between electrode locations. The small hydraulic gradient and a stable groundwater table allowed the groundwater level to be included at the fixed elevation of 13.0 m above sea level. The additional region in the ERT mesh was included to allow fine discretization (maximum 0.5 m^3 cell size) in the volume of interest, while keeping computer memory requirements and run time manageable. The inversion mesh included a total number of parameter 160,000 cells that were refined to 1,250,000 cells for the forward calculation.

Data from the time of the beginning of the CO_2 injection (day 0) were inverted to retrieve the undisturbed subsurface resistivity distribution without any effect of the CO_2 . The open source ERT modeling and inversion package BERT (Günther et al., 2006; Rücker et al., 2006) was used for the inversion. The time-lapse error estimated as part of the interpolation (Section 3.3.2) includes uncertainties within the time-series, but does not include ERT specific noise such as numerical errors in the forward modeling, coupling problems, or inexact electrode positions. For these reasons a baseline error of 3% was added to the estimated time-lapse error, resulting in a median error of 4.0%. The data were weighted with the inverse of these estimated errors. A first order smoothness regularization, where the resistivity differences between adjacent cells was minimized, was used in the inversion. This

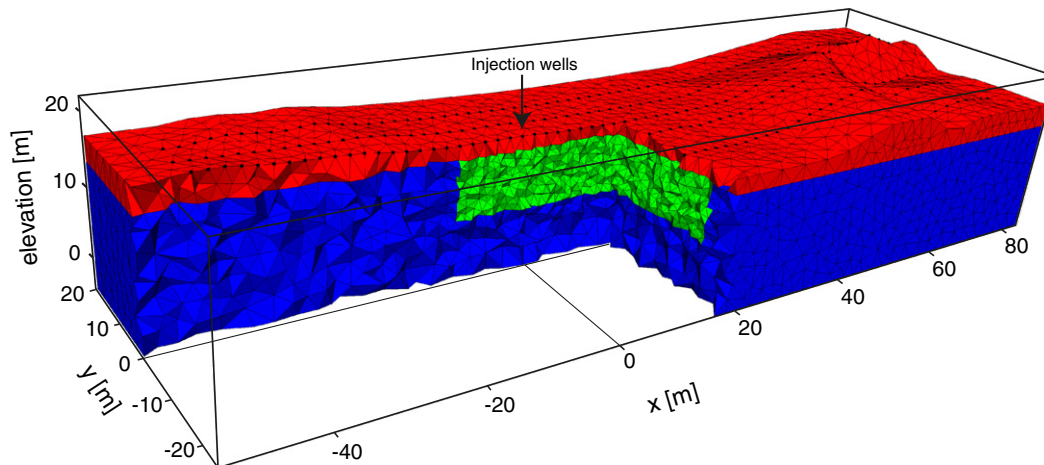


Fig. 7. Unstructured ERT parameter mesh. Three zones were distinguished in the meshing: The unsaturated zone (red), the saturated aquifer in the region and downstream from the injection wells (green) and the rest of the saturated aquifer that is not expected to be influenced by the injected CO_2 (blue). It was important to choose a high-resolution zone with small cell sizes within the aquifer in order to resolve the CO_2 plume in detail, while keeping the mesh size manageable.

regularization constraint was applied 10 times stronger in the horizontal than in the vertical direction to honor the layered geology. The inversion converged to a normalized RMS of 1 in four iterations.

The resulting baseline resistivity model \mathbf{m}_{bg} (Fig. 8) shows a top layer with very high resistivities ($>1000 \Omega\text{m}$) above the groundwater table, intermediate resistivities of 300–500 Ωm in the saturated zone down to an elevation of 5 m and low resistivities below 5 m elevation. The high resistivities in the unsaturated zone indicate that the aeolian sand holds only small amounts of pore water. The surface undulations between $x = 40\text{--}80$ m are sand dunes that have no influence on the groundwater table or flow. The intermediate resistivities between elevations of 5 and 13 m indicate the fully water saturated glacial and aeolian sands. This zone is the target for the CO_2 injection. The low resistivities below the elevation of 5 m mark the marine sands that contain more conductive groundwater (see Fig. 4 in Cahill et al., under review).

4.2. Time-lapse ERT inversions

In contrast to the baseline ERT inversion that aims at recovering the subsurface resistivity distribution, time-lapse inversions aim at imaging the changes in subsurface resistivity. These changes over time are typically much smaller than resistivity variations between different geological units and development of time-lapse inversion strategies is an active field of research. We use the methodology of Doetsch et al. (2012b) that is a combination of the difference inversion approach of LaBrecque and Yang (2001) and the ratio inversion approach of Daily et al. (1992). We invert the logarithm of the corrected data

$$\tilde{\mathbf{d}}(t) = \frac{\mathbf{d}(t)}{\mathbf{d}(t=0)} \mathbf{g}(\mathbf{m}_{bg}), \quad (1)$$

with the data $\mathbf{d}(t)$ at time t and the forward response from the baseline model $\mathbf{g}(\mathbf{m}_{bg})$. Multiplying $\mathbf{d}(t)$ with the ratio of the baseline response $\mathbf{g}(\mathbf{m}_{bg})$ and data at time $t = 0$ ensures that only relative changes in the data are inverted. Removing the baseline misfit thereby removes a large part of the error, originating both from the ERT data (e.g., electrode positions) and numerical errors in the forward model. The time-lapse inversion calculates updates to the baseline model using changes in the data.

Inversion tests with a few selected time-steps and different 2-D and 3-D approaches showed that both the inversion mesh and the time-lapse regularization are critical for good inversion results. Especially for 3-D inversions, with generally larger parameter cells than in 2-D, it

was important to include the water table in the mesh and uncouple the regularization across this boundary. Otherwise, strong resistivity variations in the unsaturated zone due to e.g., rainfall events made imaging of the CO_2 plume almost impossible. While the near-surface effects could not be removed from the data, including a vadose zone layer allowed for high-quality results to be obtained within the aquifer. Results were much improved by including a high-resolution zone in the region of main interest.

We use the 7713 preprocessed $\mathbf{d}(t)$ time-series to invert for changes to the baseline resistivity distribution shown in Fig. 7. Daily data snapshots are extracted using the geostatistical interpolation (Section 3.3.2), along with the estimated time-lapse error that is added to an error floor of 1%. The error floor of 1% assures numerical stability by avoiding overweighting of few data points and is smaller than the 3% error floor in the baseline inversion (because the modeling error is partly removed by the ratio inversion).

Tests with different model regularization showed the importance of the time-lapse regularization choice. We found that it was best always to start the inversion from the baseline model \mathbf{m}_{bg} and use a regularization that enhances smoothness of the model update and simultaneously minimizes the distance to \mathbf{m}_{bg} . By minimizing the distance to the baseline model, only changes that are necessary to fit the data are included in the model update. All time-lapse inversions converge to a model that explains the data within the estimated error within 4 iterations (normalized RMS of 0.62–1.04).

5. Results, interpretation and discussion

5.1. Time-lapse ERT results

2-D cuts through the 3-D inversion result along the center profile are shown in Fig. 9a, c and e. These images show the time-lapse results for three representative times, normalized by the baseline inversion model, so that a resistivity ratio of 1 corresponds to no change in resistivity, a ratio <1 corresponds to a decrease in resistivity, and a resistivity ratio >1 illustrates an increase of resistivity with time. All three images (Fig. 9a, c and e) show an increase in resistivity (red zones) close to the surface. These near-surface variations reflect the varying water saturation in the unsaturated sand due to drying and precipitation events and are not related to our experiment. As an example, at a water saturation of 20%, a decrease in saturation by 5% already causes an increase in resistivity by 30%, using Archie's second law (Archie, 1942) with a

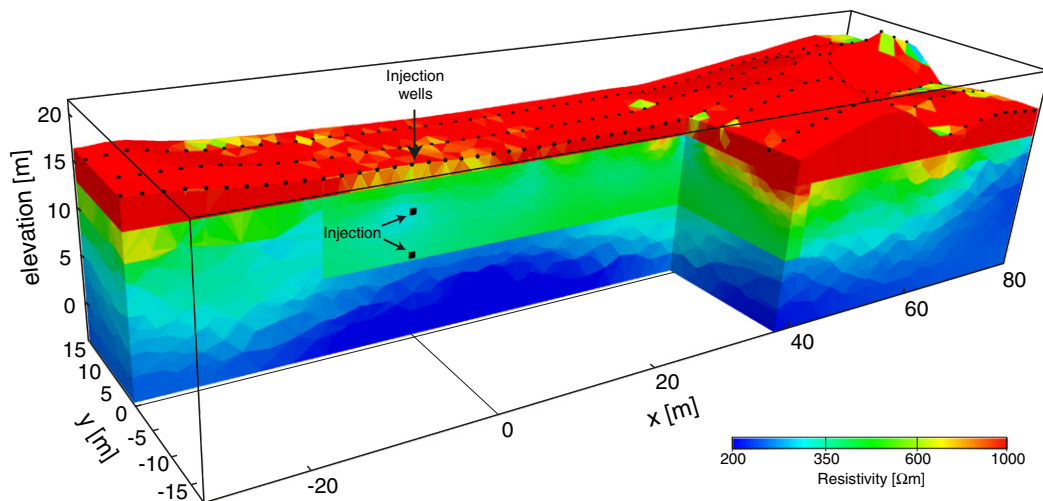


Fig. 8. Baseline ERT inversion before the beginning of the injection. The subsurface material consists of aeolian and glacial sands with varying amounts of clays and gravel. The high resistivities close to the surface indicate the unsaturated zone, with the water table at 2 m depth. Resistivity differences below the water table are due to variations in grain size, porosity, clay content and background water resistivity.

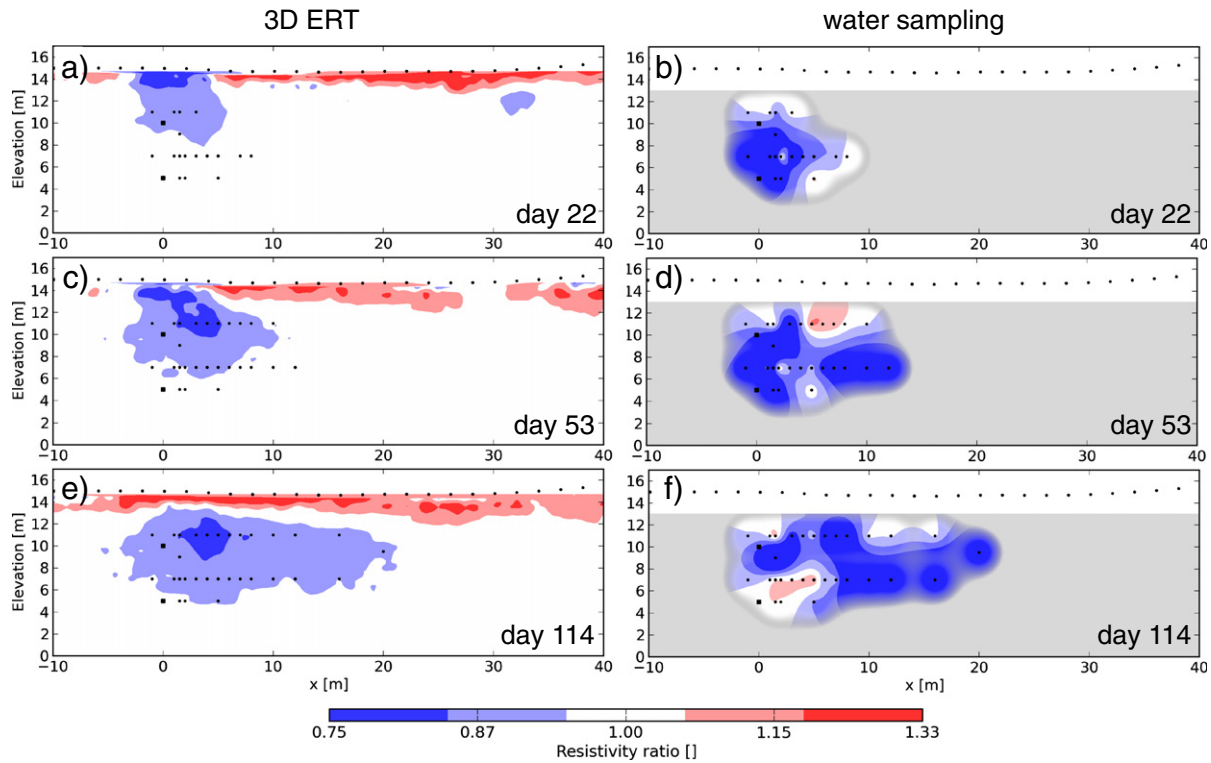


Fig. 9. Time-lapse ERT inversion results (left panels) and water sampling evaluated by kriging (right panels) for day 22 (a, b), 53 (c, d) and 114 (e, f) after the beginning of the CO₂ injection. The images show a cut through the 3-D models at the center profile, with the injection points at $x = 0$. Dots at the surface indicate electrodes, dots in the subsurface indicate EC sampling locations and black squares mark the injection points. EC shows a lot of detail at the sampling points, but is unable to define the extent of the plume. ERT has lower resolution, but can fully image the plume.

saturation exponent of 2. The ground was generally quite wet during the acquisition period, due to frequent precipitation (see Fig. 3b). This means that during dry periods, the sandy soil can easily drain so that water saturation decreases by 5–10%. These near surface variations were partly masking the resistivity variations within the aquifer and only a combination of very fine discretization, decoupling at the groundwater level and regularization including minimization of the update to m_{bg} enabled imaging of the dissolved CO₂ plume.

The near-surface decrease in resistivity above the injection points at $x = 0$ is however related to the CO₂ and its high injection rate at the beginning of the experiment. We interpret this decrease in resistivity to be due to an increase in water saturation, caused by escaping gaseous CO₂. The initial CO₂ injection rate was too high for the CO₂ to be dissolved, so that bubbles of gaseous CO₂ migrated upwards and escaped to the atmosphere. This escaping CO₂ displaced moisture and some of the water in the aquifer, pushing it into the unsaturated zone. The actual amount of water was probably very small, but as mentioned above, at a water saturation of 20%, an increase in saturation by 5% already causes a decrease in resistivity by 30%. The effect of the decreased resistivity above the injection well is becoming weaker with time and cannot be observed in the last image at day 114 after the injection (Fig. 9e).

Below the strong variations in the near-surface, one can clearly see the dissolved CO₂ as a decrease in resistivity in Fig. 9a, c and e. The images show how the plume migrates and disperses with the groundwater flow. The dissolved CO₂ moves mostly between a depth of 4 and 6 m and can be imaged until the end of the experiment at day 120. While the 2-D slices show the evolution of the CO₂ plume along the center profile, the main strength of the electrical monitoring is the 3-D imaging of the plume, as illustrated by Fig. 10. The CO₂ plume, which is here defined by a threshold of a 7% decrease in resistivity (resistivity ratio of 0.93) spreads not only in the direction of the groundwater

flow, but also extends to a width of approximately 10 m in the direction perpendicular to the groundwater flow. Interesting is also the finger that extends from the main plume in southeastward direction, which could mark a preferential flow path.

5.2. Comparison with electrical resistivity groundwater sampling

Before and during the CO₂ injection experiment, groundwater electrical resistivity was measured on samples extracted from 29 wells (Cahill et al., under review). The timing of the sampling campaigns is marked as dashed lines in Fig. 3. These water resistivity measurements give a unique possibility to compare the ERT results with in situ data. Because the groundwater sampling measures the resistivity of the water only and ERT recovers the resistivity of the full subsurface including water and matrix, the absolute resistivity values from the two methods cannot be compared. For time-lapse analysis however, the two data types can be compared by evaluating the relative change in resistivity. Assuming that the rock matrix is non-conductive, relative changes to the groundwater resistivity will induce the same relative changes for the subsurface resistivity.

In order to compare the water resistivity samples with the ERT results, we first normalize all water resistivities by their values measured before the beginning of the CO₂ injection. For the visualization, we then interpolate the normalized water resistivities using kriging. We use an exponential model with a range of 3.6 m that was fitted to the experimental variogram; the interpolation was restricted to the saturated aquifer. The resulting normalized resistivity images along the central ERT profile are shown in Fig. 9b, d and f. Regions away from the sampling points are shown in gray, based on the uncertainty estimation of the kriging.

Comparison with the ERT images shows that the two methods generally image the CO₂ in the same region. There are, however,

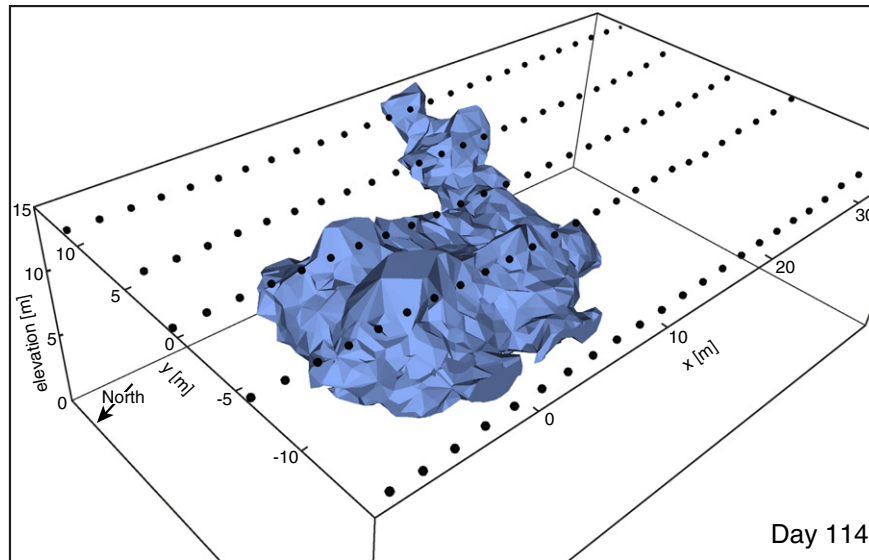


Fig. 10. 3-D rendering of the CO₂ plume at day 114 after the start of injection. The plume is extracted from the time-lapse 3-D ERT inversion result by setting a threshold of 7% decrease in resistivity (resistivity ratio of 0.93) compared to the baseline model.

some significant differences. In general, the water samples show a stronger change in resistivity. This is not surprising, because the regularization in the ERT inversions favors models that can explain the data with as little change as possible. Other possible regularizations using robust (L1-type, e.g., Farquharson, 2008) model norms or focused inversions (Rosas Carbajal et al., 2012; Vignoli et al., 2013) could help to recover the true amplitude of the change in resistivity. The smaller amplitude of the change in the ERT results also leads to smaller plumes in the ERT images, due to the same color scale being used for both data types. This might make the plume appear smaller in the ERT images and lead to underestimation of the traveled distance of the plume front.

The strength of the ERT is the three-dimensional sensitivity distribution over the entire survey area. The CO₂ plume can thus be characterized in three dimensions and especially the outline of the plume can be detected in the larger than 100 × 25 m area. Water sampling is more accurate at the measurement locations, but in an actual application it would not be feasible with such a high spatial density of water samples. The resistivity distribution at days 53 and 114 (Fig. 9d and f) show fine detail within the sampling area, but it is not possible to judge how far downstream the dissolved CO₂ has moved, because the farthest downstream sampling points already detect an increased EC. Also, migration of the CO₂ in even a slightly different direction or transport through preferential flow paths cannot be detected. By contrast, Fig. 10 demonstrates how ERT can recover the 3-D shape of the plume, including the zone in the southwest, which could potentially be a preferential flow path.

5.3. Surface ERT monitoring of leaking CO₂

The results presented here clearly show the potential of surface ERT monitoring of CO₂ in shallow aquifers. Taking this to large industry scale monitoring of leakage from CO₂ reservoirs is possible if attention is given to the following:

- *Long term monitoring:* While our project covered a third of a year, monitoring of potential leakage from deep CO₂ storage reservoirs will have to be active for several years or even decades. This calls for development of a fully automated data processing and inversion system wrapping the algorithms outlined in this paper. In addition, stable measurements of data are necessary in order to stack data to a sufficiently low noise level.

- *Covered area:* While we concentrated on an area of 126 × 25 m, CO₂ storage reservoirs on industry scale will extend to several square kilometers. Covering e.g., a square kilometer in 3-D with permanently installed electrodes and a target depth of 100–150 m is possible with existing hardware. Full switching capability between electrodes is desirable, but this study has shown that sufficient coverage can be obtained by switching in and out entire cables. The simpler setup greatly reduces costs.
- *Sources of resistivity changes:* The unsaturated-zone variations in this study demonstrate that other sources of resistivity changes can make it difficult to identify leaking CO₂. This problem will be amplified in long-term studies and calls for monitoring of precipitation, temperature and soil moisture using off the shelf instrumentation. Also, it is crucial for the interpretation of the ERT data to have access to a network of screens with continuous water sampling and chemical analysis.
- *Induced polarization:* Induced polarization might be closely related to the chemical reactions at the grain surfaces. We have not shown results from the induced polarization data also collected, but this is the subject of ongoing research. In a large-scale setup with very long cables it will be necessary to separate potential and current cables in order to avoid capacitive coupling.
- *Geochemical reactions:* While electrical conductivity (or resistivity) was found to be the most reliable indicator for CO₂ at our field site (Cahill and Jakobsen, 2013), this might not be the case in other aquifers (Dafflon et al., 2013). The resistivity response to dissolved CO₂ needs to be carefully assessed for each aquifer and geological situation.

These challenges are critical for detecting dissolved CO₂ in potable aquifers. The situation is different for monitoring of supercritical CO₂ using crosshole ERT. In this case, the electrical signal is stronger and easier to predict, but electrode installation and cabling might be problematic (Carrigan et al., 2013; Doetsch et al., 2013; Schmidt-Hattenberger et al., 2013). Also, crosshole ERT has a very limited areal coverage and cannot be used to monitor leakage over large areas from underground well zones.

6. Conclusions

A CO₂ injection experiment in a shallow aquifer has been monitored with surface ERT. The CO₂ was injected for 72 days into a potable aquifer

at 5 and 10 m depth and monitored using 320 electrodes installed on a surface grid of 126 × 25 m size. An advanced computer-controlled setup enabled fully automatic switching between subsets of the 320 electrodes, acquisition of ERT data and data upload into an online database. Data was acquired for 120 days, with some gaps in the data acquisition caused by intermittent instrument failure. These gaps in the ERT time-series compromised the overall data quality, but geostatistical interpolation (kriging) was found to be able to fill the data gaps and estimate reasonable time-lapse errors for the inversion.

For the 3-D time-lapse ERT inversion, we found that the unstructured mesh was critical for imaging the dissolved CO₂ plume. The best results were obtained using a 3-region mesh that includes the unsaturated zone, a high-resolution zone for the CO₂ plume and a region covering the rest of the saturated aquifer. This mesh enabled high resolution of the plume, while keeping computer run time and memory requirements manageable. The time-lapse update was always calculated with respect to the baseline model of the undisturbed aquifer and the time-lapse regularization choice was found to be very important. We found that a combination of minimization of the lateral variation (smoothing) and minimization of the variation from the baseline model gave the best results.

The time-lapse inversion results clearly show the plume of dissolved CO₂ as a decrease in electrical resistivity, while resistivities in the unsaturated zone mostly increase, due to drying sand. The CO₂ plume and its outline can be followed in 3-D for the full 120-day duration. The CO₂ plume is found to move mostly in the anticipated groundwater flow direction, but also shows some spreading in other directions and a possible preferential flow path. The ERT results generally agree with results from water resistivity samples taken in 29 wells in the survey area. The water samples show more detail in the sampled well field and ERT is superior in outlining the plume in 3-D, especially once it left the well field.

Our results clearly show that electrical resistivity monitoring can detect dissolved CO₂ in potable aquifers and image the shape and development of the CO₂ plume. Challenges for detection of leakage from deep CO₂ storage include long monitoring times and large survey areas that will be necessary. Future work will also be necessary on the electrical signature of geochemical changes induced by CO₂.

Acknowledgments

The authors would like to thank the field crew for their paramount effort of installing and continuously maintaining the ERT equipment. We would like to thank James Ramm and Daniel Kingo Løve for their initial processing of the data and technician Simon Ejlertsen and software developer Philippe Gazoty for their large effort in getting the system up and running and figuring out workarounds on the parts of the system, which we had not developed. Finally Professor Kurt Sørensen came up with the idea for the simple design of the electrode switching boxes, which were essential for carrying out the experiment. This study was conducted as part of the CO₂-GS project (<http://co2gs.geus.net/>) funded by the Danish Strategic Research Council. Two anonymous reviewers helped to greatly improve the clarity of the paper.

References

- Ajo-Franklin, J.B., Peterson, J., Doetsch, J., Daley, T.M., 2013. High-resolution characterization of a CO₂ plume using crosswell seismic tomography: Cranfield, MS, USA. *Int. J. Greenh. Gas Control* 18, 497–509.
- Archie, G.E., 1942. The electrical resistivity log as an aid in determining some reservoir characteristics. *Trans. Am. Inst. Min. Metall. Pet. Eng.* 146, 54–62.
- Benson, S.M., Cook, P.J., et al., 2005. Underground geological storage of carbon dioxide. In: Metz, B., Davidson, O., Coninck, H.d., Loos, M., Meyer, L. (Eds.), Chapter 5, Intergovernmental Panel on Climate Change Special Report on Carbon Dioxide Capture and Storage. Cambridge University Press.
- Binley, A., Cassiani, G., Middleton, R., Winship, P., 2002. Vadose zone flow model parameterisation using cross-borehole radar and resistivity imaging. *J. Hydrol.* 267 (3–4), 147–159.
- Birkholzer, J.T., Zhou, Q., Tsang, C.-F., 2009. Large-scale impact of CO₂ storage in deep saline aquifers: a sensitivity study on pressure response in stratified systems. *Int. J. Greenh. Gas Control* 3 (2), 181–194.
- Cahill, A.G., Jakobsen, R., 2013. Hydro-geochemical impact of CO₂ leakage from geological storage on shallow potable aquifers: a field scale pilot experiment. *Int. J. Greenh. Gas Control* 19, 678–688. <http://dx.doi.org/10.1016/j.jggc.2013.03.015>.
- Cahill, A.G., Marker, P., Jakobsen, R., 2013w. Hydrogeochemical and mineralogical effects of sustained CO₂ contamination in a shallow sandy aquifer: a field scale controlled release experiment. *Water Resour. Res.* (under review).
- Carrigan, C.R., Yang, X., Labrecque, D.J., Larsen, D., Freeman, D., Ramirez, A.L., Daily, W., Aines, R., Newmark, R., Friedmann, J., Hovorka, S., 2013. Electrical resistance tomographic monitoring of CO₂ movement in deep geologic reservoirs. *Int. J. Greenh. Gas Control* 18, 401–408.
- Cassiani, G., Bruno, V., Villa, A., Fusi, N., Binley, A.M., 2006. A saline trace test monitored via time-lapse surface electrical resistivity tomography. *J. Appl. Geophys.* 59 (3), 244–259.
- Coscia, I., Linde, N., Greenhalgh, S., Vogt, T., Green, A., 2012. Estimating traveltimes and groundwater flow patterns using 3D time-lapse crosshole ERT imaging of electrical resistivity fluctuations induced by infiltrating river water. *Geophysics* 77 (4), E239–E250.
- Dafflon, B., Wu, Y., Hubbard, S.S., Birkholzer, J.T., Daley, T.M., Pugh, J.D., Peterson, J.E., Trautz, R.C., 2013. Monitoring CO₂ intrusion and associated geochemical transformations in a shallow groundwater system using complex electrical methods. *Environ. Sci. Technol.* 47 (1), 314–321.
- Daily, W., Ramirez, A., Labrecque, D., Nitao, J., 1992. Electrical resistivity tomography of vadose water movement. *Water Resour. Res.* 28 (5), 1429–1442.
- Doetsch, J., Linde, N., Pessognelli, M., Green, A.G., Gunther, T., 2012a. Constraining 3-D electrical resistance tomography with GPR reflection data for improved aquifer characterization. *J. Appl. Geophys.* 78, 68–76.
- Doetsch, J., Linde, N., Vogt, T., Binley, A., Green, A.G., 2012b. Imaging and quantifying salt-tracer transport in a riparian groundwater system by means of 3D ERT monitoring. *Geophysics* 77 (5), B207–B218.
- Doetsch, J., Kowalsky, M.B., Doughty, C., Finsterle, S., Ajo-Franklin, J.B., Carrigan, C., Yang, X., Hovorka, S.D., Daley, T.M., 2013. Constraining CO₂ simulations by coupled modeling and inversion of electrical resistance and gas composition data. *Int. J. Greenh. Gas Control* 18, 510–522.
- Farquharson, C.G., 2008. Constructing piecewise-constant models in multidimensional minimum-structure inversions. *Geophysics* 73 (1), K1–K9.
- Giese, R., Hennings, J., Lüth, S., Morozova, D., Schmidt-Hattenberger, C., Würdemann, H., Zimmer, M., Cosma, C., Juhlin, C., 2009. Monitoring at the CO₂ SINK site: a concept integrating geophysics, geochemistry and microbiology. *Energy Procedia* 1 (1), 2251–2259.
- Günther, T., Rücker, C., Spitzer, K., 2006. Three-dimensional modelling and inversion of dc resistivity data incorporating topography – II. Inversion. *Geophys. J. Int.* 166 (2), 506–517.
- Günther, T., Ronczka, M., Rücker, C., 2013. Long electrode ERT for salt water monitoring-modelling. Sensitivity and Resolution. Near Surface Geoscience, Bochum, Germany.
- Hermans, T., Vandenbohede, A., Lebbe, L., Nguyen, F., 2012. A shallow geothermal experiment in a sandy aquifer monitored using electric resistivity tomography. *Geophysics* 77 (1), B11–B21.
- Hovorka, S.D., Benson, S.M., Doughty, C., Freifeld, B.M., Sakurai, S., Daley, T.M., Kharaka, Y.K., Holtz, M.H., Trautz, R.C., Nance, H.S., Myer, L.R., Knauss, K.G., 2006. Measuring permanence of CO₂ storage in saline formations: the Frio experiment. *Environ. Geosci.* 13 (2), 105–121.
- Hovorka, S.D., Meckel, T.A., Trevino, R.H., Lu, J., Nicot, J.-P., Choi, J.-W., Freeman, D., Cook, P., Daley, T.M., Ajo-Franklin, J.B., Freifeld, B.M., Doughty, C., Carrigan, C.R., Brecque, D.L., Kharaka, Y.K., Thordsen, J.J., Phelps, T.J., Yang, C., Romanak, K.D., Zhang, T., Holt, R.M., Lindler, J.S., Butsch, R.J., 2011. Monitoring a large volume CO₂ injection: year two results from SECARB project at Denbury's Cranfield, Mississippi, USA. *Energy Procedia* 4, 3478–3485.
- Kemma, A., Kulesa, B., Vereecken, H., 2002. Imaging and characterisation of subsurface solute transport using electrical resistivity tomography (ERT) and equivalent transport models. *J. Hydrol.* 267 (3–4), 125–146.
- Kitanidis, P., 1997. Introduction to Geostatistics: Applications in Hydrogeology. Cambridge University Press.
- Labrecque, D.J., Yang, X., 2001. Difference inversion of ERT data: a fast inversion method for 3-D in situ monitoring. *J. Environ. Eng. Geophys.* 6 (2), 83–89.
- Lamert, H., Geistlinger, H., Werban, U., Schutze, C., Peter, A., Hornbruch, G., Schulz, A., Pohlert, M., Kalia, S., Beyer, M., Grossmann, J., Dahmke, A., Dietrich, P., 2012. Feasibility of geoelectrical monitoring and multiphase modeling for process understanding of gaseous CO₂ injection into a shallow aquifer. *Environ. Earth Sci.* 67 (2), 447–462.
- Nicot, J.-P., 2008. Evaluation of large-scale CO₂ storage on fresh-water sections of aquifers: an example from the Texas Gulf Coast Basin. *Int. J. Greenh. Gas Control* 2 (4), 582–593.
- Pebesma, E.J., Wesseling, C.G., 1998. Gstat: a program for geostatistical modelling, prediction and simulation. *Comput. Geosci.* 24 (1), 17–31.
- Robert, T., Caterina, D., Deceuster, J., Kaufmann, O., Nguyen, F., 2012. A salt tracer test monitored with surface ERT to detect preferential flow and transport paths in fractured/karstified limestones. *Geophysics* 77 (2), B55–B67.
- Rosas Carbajal, M., Linde, N., Kalscheuer, T., 2012. Focused time-lapse inversion of radio and audio magnetotelluric data. *J. Appl. Geophys.* 84, 29–38.
- Rücker, C., Günther, T., Spitzer, K., 2006. Three-dimensional modelling and inversion of dc resistivity data incorporating topography – I. Modelling. *Geophys. J. Int.* 166 (2), 495–505.

- Schmidt-Hattenberger, C., Bergmann, P., Bösing, D., Labitzke, T., Möller, M., Schröder, S., Wagner, F., Schütt, H., 2013. Electrical resistivity tomography (ERT) for monitoring of CO₂ migration – from tool development to reservoir surveillance at the Ketzin pilot site. *Energy Procedia* 37, 4268–4275.
- Singha, K., Gorelick, S.M., 2005. Saline tracer visualized with three-dimensional electrical resistivity tomography: field-scale spatial moment analysis. *Water Resour. Res.* 41 (5), W05023.
- Slater, L., Binley, A.M., Daily, W., Johnson, R., 2000. Cross-hole electrical imaging of a controlled saline tracer injection. *J. Appl. Geophys.* 44 (2–3), 85–102.
- Strazisar, B.R., Wells, A.W., Diehl, J.R., Hammack, R.W., Veloski, G.A., 2009. Near-surface monitoring for the ZERT shallow CO₂ injection project. *Int. J. Greenh. Gas Control* 3 (6), 736–744.
- Vignoli, G., Fiandaca, G., Christiansen, A.V., Kirkegaard, C., Auken, E., 2013. Sharp Spatially Constrained Inversion. *Near Surface Geoscience*, Bochum, Germany.